

Temporal evolution of flux rope/tube entanglement in 3-D Hall MHD simulations

Yingdong Jia¹, Yi Qi², San Lu¹, and Christopher T. Russell¹

¹University of California Los Angeles

²University of California, Los Angeles

November 21, 2022

Abstract

At the Earth’s magnetopause, flux tubes observed by the Magnetospheric Multiscale (MMS) spacecraft in “entangled” pairs have been interpreted as a precursory stage to the formation of a new pair of flux ropes by magnetic reconnection, of which one reconnected rope joins the magnetosphere. Understanding the connectivity of these tubes before and after the entanglement is essential to understanding the transport of particles and energy between the magnetosphere and the solar wind. In this paper, we use a three-dimensional Hall MHD model to simulate the interaction of two entangled flux tubes in the ambient plasma. Four types of interactions are simulated: Two types of magnetic field geometry (flux tube-flux tube, and flux rope-flux rope) are tested separately, each under two different boundary conditions that drive the interaction. With one type of boundary condition, magnetic reconnection transforms the two tubes/ropes into new pairs. The process is performed under plasma conditions comparable to those of such events identified in recent MMS observations. The detailed 3-D evolution is shown at representative stages, with key parameters shown across the entanglement interface. The shape of the central current sheet and evolution of magnetic field curvature are also discussed. Our study supports the feasibility of reconnection between entangled flux tubes, recognizes the importance of ambient plasma conditions for the completion of such processes, and quantifies how such structures evolve to modify the solar wind-geomagnetic field interaction. In addition, this model is applicable to flux rope interactions in the solar corona.

1
2 **Temporal Evolution of Flux Rope/Tube Entanglement in 3-D Hall MHD**
3 **Simulations**

4
5 **Ying-Dong Jia¹, Yi Qi¹, San Lu¹, C. T. Russell¹**

6
7 ¹Department of Earth, Planetary and Space Sciences, University of California, Los Angeles, Los
8 Angeles, CA 90095-1567.

9
10
11 Corresponding author: Yingdong Jia (yingdong@igpp.ucla.edu)

12
13
14
15 **Key points:**

- 16
- 3-D Hall MHD used to model flux tube interactions.
 - Previously entangled flux tubes reconnect into untangled ropes.
 - This process is mainly driven by the momentum of converging plasma.
- 17
18
19

20

21 **Abstract**

22

23 At the Earth's magnetopause, flux tubes observed by the Magnetospheric Multiscale
24 (MMS) spacecraft in "entangled" pairs have been interpreted as a precursory stage to the
25 formation of a new pair of flux ropes by magnetic reconnection, of which one reconnected rope
26 joins the magnetosphere. Understanding the connectivity of these tubes before and after the
27 entanglement is essential to understanding the transport of particles and energy between the
28 magnetosphere and the solar wind. In this paper, we use a three-dimensional Hall MHD model to
29 simulate the interaction of two entangled flux tubes in the ambient plasma. Four types of
30 interactions are simulated: Two types of magnetic field geometry (flux tube-flux tube, and flux
31 rope-flux rope) are tested separately, each under two different boundary conditions that drive the
32 interaction. With one type of boundary condition, magnetic reconnection transforms the two
33 tubes/ropes into new pairs. The process is performed under plasma conditions comparable to
34 those of such events identified in recent MMS observations. The detailed 3-D evolution is shown
35 at representative stages, with key parameters shown across the entanglement interface. The shape
36 of the central current sheet and evolution of magnetic field curvature are also discussed. Our
37 study supports the feasibility of reconnection between entangled flux tubes, recognizes the
38 importance of ambient plasma conditions for the completion of such processes, and quantifies
39 how such structures evolve to modify the solar wind-geomagnetic field interaction. In addition,
40 this model is applicable to flux rope interactions in the solar corona.

41

42 **Plain Language Summary**

43

44 Magnetic flux bundles, generated by interaction between the solar wind and the geomagnetic
45 field, play an important role in the energy and momentum transfer from the Sun to the Earth.
46 These flux bundles move in the magnetosheath and can become entangled. We examine four
47 scenarios to simulate the evolution of the entanglement process under the nominal conditions of
48 the magnetosheath. Our simulations quantitatively support the hypothesis that flux tube
49 reconnection is consistent with spacecraft observations.

50

51 **1 Introduction**

52

53 Magnetic reconnection, the process in which magnetic fields of opposite polarity
54 annihilate and reconnect converting magnetic energy into kinetic energy, has long been a classic
55 topic of research in plasma physics. In addition to its ubiquity and explosive energy release, at
56 the magnetopause, the change in magnetic field topology during magnetic reconnection allows
57 particles from the solar wind and the magnetosphere to mix. Such mixing, as well as the
58 topological change itself, is believed to be the major channel for mass and momentum exchange
59 on a global scale.

60

61 On the day side of the magnetosphere, magnetic reconnection is often associated with a
62 commonly observed phenomenon called the flux transfer event (FTE), characterized by the
63 magnetic field in the form of a magnetic flux rope (Russell & Elphic, 1979). Four different
64 theories have been proposed to reconstruct/generate their global topologies, and it is not yet
65 observationally settled which mechanism is operative. Three mechanisms are summarized by
66 Fear et al.'s (2008) Figure 1: The original connected flux rope model (Russell and Elphic, 1979);
the magnetic island model, often called the multiple X-line model (Lee and Fu 1985); and the

67 outflow-region bubble model (Southwood et al., 1988). A fourth type is the proposed magnetic
68 reconnection induced by flow vortices, such as modeled by Dorelli and Bhattacharjee (2009),
69 and supported by a number of observations (Liu and Hu, 1988; Zhang et al., 2011; and
70 references therein).

71 Numerous modeling efforts have attempted to self-consistently generate FTEs in a global
72 3-D magnetosphere to understand their formation, including MHD models relying on ad hoc or
73 numerical resistivity to initiate magnetic reconnection (e.g., Fedder et al., 2002; Raeder, 2006),
74 and a hybrid particle-fluid model (Tan et al., 2011). These mostly favor the magnetic island
75 explanation (Lee and Fu, 1985).

76 With the launch of the Magnetospheric Multiscale (MMS) mission in 2015, in situ
77 plasma and field measurements at the magnetosphere with high time and spatial resolution have
78 become available at the corners of a tetrahedron with side length as small as 7km (Burch et al.,
79 2015). Magnetic reconnection processes are now being extensively studied using the MMS data
80 (cf. Burch et al., 2016).

81 As part of the magnetic reconnection studies enabled by the MMS measurements, FTEs
82 have been substantially studied in recent years: One statistical study found FTEs either filled
83 with or devoid of hot magnetospheric particles (Zhao, 2019). A complementary study showed
84 FTEs to be entangled with each other (Øieroset et al., 2019). These two phenomena in turn led to
85 the hypothesis that FTEs were not created singly but, as some previous numerical models have
86 visualized, at multiple sites on the magnetosphere. The originally disparate flux tubes then
87 collide and merge, producing a pair of flux ropes, via a second round of magnetic reconnection
88 (Russell & Qi, 2020). Following this hypothesis, multiple cases consistent with the early, middle,
89 and late stages of time evolution of such FTE reconnections have been identified in the MMS
90 data obtained between 2015 and 2018 (Qi et al., 2020).

91 The realization of the importance of FTE entanglement is not new. In theoretical
92 treatments, “interlinked” flux tubes have been repeatedly depicted since the pioneering
93 visualization work by Hesse et al. (1990), using analytical functions of prescribed currents, and
94 sketched by Otto et al. (1991), based on multiple MHD simulation results. Later, in more
95 sophisticated models, magnetic field lines underwent multiple reconnection and produced flux
96 ropes in which all magnetic field connectivity options were possible. The Cluster observation of
97 time evolution with a resolution of a few minutes (Pu et al., 2013) appeared to be consistent with
98 the interlinking theory. In contrast, new events found in MMS observations consist of
99 compression on both sides with a current sheet in the middle. This configuration is consistent
100 with two magnetic flux tubes merging at their interface (Øieroset et al., 2019; Qi et al., 2020). In
101 this paper, we have designed a numerical local-interaction model that shows the 3-D evolution of
102 such entangled FTE reconnection with several distinctive conditions. Following this introductory
103 section, section 2 explains our model and numerical methods, and section 3 shows our results,
104 while section 4 summarizes this paper with discussion and applications.

105

106 **2. Model Description**

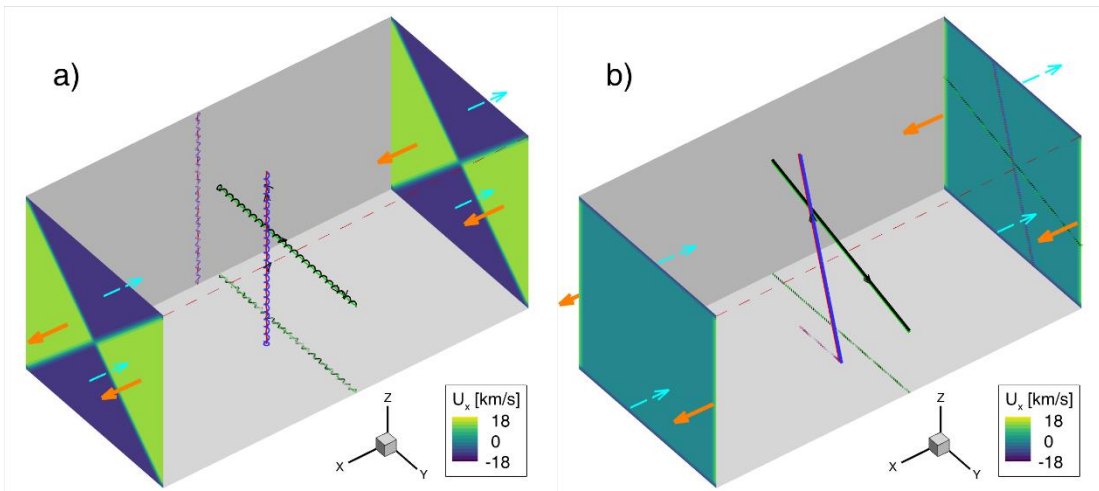
107

108 In their Figure 4, Russell & Qi (2020) show a sketch of the interaction between two flux
109 ropes. Panel b describes the active entanglement stage which is consistent with MMS
110 observations, with reconnection signatures at the interface. Panel c illustrates the final product of
111 entanglement: a new pair of disentangled flux ropes. Following this idea, our study simulates a

112 flux rope-flux rope interaction, and then extends to a more general situation: flux tube
 113 interactions with no initial twist in the field. Two different driving mechanisms as described
 114 below provide us with four different interaction scenarios in total.
 115

2.1 The physical models of the four simulation cases

116
 117
 118 To examine this process, we employ a Cartesian calculation domain of $51.2 \times 25.6 \times 25.6$
 119 R_E . The x-axis is along the initial flow direction, while y and z are two arbitrary right-hand
 120 orthogonal directions for the initial flux-rope alignment. As shown in Figure 1, we place two flux
 121 ropes perpendicular to each other, at $d_0 = \pm 1.5 R_E$, respectively. Initially, the plasma density and
 122 temperature are a uniform $10 / \text{cc}$ and $2 \times 10^7 \text{ K}$, respectively, which is similar to the background
 123 conditions during the entanglement event on Nov 07, 2015 (Russell and Qi, 2020). We refer to
 124 this event as the Nov07 event hereafter. This condition approximates a sound speed of $V_s \sim$
 125 520 km/s , ion thermal velocity of 300 km/s , and an ion inertial length of 70 km , or $0.01 R_E$. The
 126 background magnetic field is 0 nT , and the flow velocity is 0 km/s , except as defined by the
 127 initial conditions (ICs) and boundary conditions (BCs).
 128



129
 130 **Figure 1.** Two types of initial and boundary conditions of the simulation domain plotted in 3-D
 131 view. Left panel a): Case A1, magnetic flux ropes at the center, forced flow for both the initial
 132 condition and at the $x = \text{max/min}$ boundary. Right panel b): Case B2, flux tubes at the center,
 133 dragged by the flow at the side boundary. Colored lines in the middle are indicative of magnetic
 134 field lines. Their projections are shown on two surfaces with dashed lines of the same color.
 135 Orange and cyan arrows mark the flow directions at the root of the arrow.
 136

137 Initially, we use the force-free cylindrical model to simulate each of the two flux ropes
 138 (Lundquist, 1950):
 139

$$140 \quad B_{r'} = 0, B_{\phi'} = H B_0 J_1(\alpha r' / R_0), B_{z'} = B_0 J_0(\alpha r' / R_0) \text{ when } r' \leq R_0, B = 0 \text{ when } r' > R_0 \quad (1)$$

141
 142 where r' , ϕ' and z' are local poloidal coordinates with z' being the direction of the axis of the
 143 flux rope, $H = \pm 1$ is the handedness, or chirality of the helical magnetic vectors, J_0 and J_1 are the

144 0^{th} and 1^{st} order Bessel functions, R_0 is the radius of the flux rope, and constant $\alpha=2.405$ defines
 145 the ratio between azimuthal component and axial component (Imber et al., 2014).

146 In MMS observations, an entanglement event typically lasts 10 to 100 seconds, in a 100
 147 km/s magnetic sheath flow (Qi et al., 2020), so the average radius of one of the two compressed
 148 flux ropes is about $0.25 R_E$, smaller than that of a stand-alone FTE measured and modeled in pre-
 149 MMS era models, which may extend up to a few R_E . In this study, we set the radius $R_0 = 0.4 R_E$,
 150 which is between the recently observed ion-scale FTE size and the size used in traditional
 151 models. The coordinate conversion from local cylindrical to Cartesian coordinates is achieved by
 152 rotating z' to the desired direction: For flux rope #1, z' is parallel to the Cartesian z -axis, and
 153 displaced by $d_1 = 1.5 R_E$ along the x -axis, while for flux rope #2, z' is parallel to the y -axis, and
 154 displaced by $d_2 = -1.5 R_E$ along the x -axis. After the real-time simulation has started, the two
 155 flux tubes are driven against each other by boundary conditions so that they become entangled.

156 As summarized in Table 1, two types of initial conditions are adopted based on equation
 157 (1): The initial conditions of each of the flux ropes in case 1 are defined by equation (1), while
 158 the flux tubes with case 2 initial conditions were modified from equation (1) by setting $B\phi'=0$. In
 159 addition, both flux tubes with case 2 initial conditions are tilted inside the y - z plane by an angle
 160 of 16.7° , away from each other, to facilitate reconnection. For the plasma inside the tubes of all
 161 cases, a constant bulk flow velocity of $u_0 = -\text{sign}(d_i) \times 13\text{km/s}$ is assigned along the x -axis, where
 162 subscript i runs through flux ropes 1 and 2.

163 As also summarized in Table 1, two different boundary conditions are applied to move
 164 the magnetic flux tubes: Case A simulates two flux ropes/tubes being pushed against each other
 165 by the dynamic pressure of the ambient plasma. Cases A1 and A2 divide the entire domain into
 166 four regions, and use both the initial and boundary conditions to maintain the flow with speed u_0
 167 in these regions, respectively. Specifically, as plotted in Figure 1a, both $x=x_{\min}$ and $x=x_{\max}$
 168 boundaries have inflow and outflow conditions. On the other four sides, where y and z are at
 169 their minimum and maximum values, floating boundaries are applied, where the boundary value
 170 equals the value in its adjacent cell located in the opposite direction of the boundary normal.
 171 Accordingly, this floating boundary is a zero-gradient boundary.

172 The case B boundary simulates two flux ropes/tubes being pulled against each other, i.e.
 173 the interaction is driven by magnetic tension force exerted from the distant end of the flux
 174 ropes/tubes. Cases B1 and B2 employ velocity u_0 at both ends of the flux ropes/tubes as a side
 175 boundary condition, while the plasma outside the tubes is initially stationary. Specifically, both
 176 y -boundaries force a flow of $+u_0$ in the $+x$ direction, while both z -boundaries are fixed with a
 177 flow of $-u_0$. Accordingly, both x boundaries are floating boundaries, to allow inflow, outflow,
 178 and stationary conditions determined by their location, as shown in Figure 1b.

179
 180 **Table 1.** Comparison of the four cases presented in this study: Each is a combination of two
 181 types of initial conditions and two types of boundary conditions.

	BC case A Dynamic pressure	BC case B Tension force
IC type 1: Flux rope	Case A1	Case B1
IC type 2: $B\phi = 0$ Flux tube	Case A2	Case B2

183

184

2.2 The Hall-MHD equations and numerical solver

The ideal MHD model of localized plasma interaction solves for the continuity, momentum, and pressure of the proton-electron plasma, as well as the magnetic induction equation. In addition, Hall terms (Tóth et al., 2008) are added to guarantee a fast reconnection that is achievable by particle-fluid hybrid models or full particle models (Birn et al., 2001). The full set of control equations are written as:

$$\frac{\partial \rho}{\partial t} + \nabla \cdot (\rho \mathbf{u}) = 0 \quad (2)$$

$$\rho \frac{\partial \mathbf{u}}{\partial t} + \rho (\mathbf{u} \cdot \nabla) \mathbf{u} = -\nabla P + \mathbf{G} + en\mathbf{E} \quad (3)$$

$$\frac{\partial P}{\partial t} + (\mathbf{u} \cdot \nabla) P + \gamma P (\nabla \cdot \mathbf{u}) = \mathbf{G} \mathbf{u} + \eta \mathbf{J}^2 \quad (4)$$

$$\frac{\partial \mathbf{B}}{\partial t} = -\nabla \times \mathbf{E} \quad (5)$$

$$\mathbf{E} = \mathbf{E}_0 - \mathbf{u} \times \mathbf{B} + \eta \mathbf{J} + \frac{\mathbf{J} \times \mathbf{B}}{en} \quad (6)$$

where e is the electric charge on an electron; ρ , \mathbf{u} , P is the mass density, bulk velocity vector and thermal pressure of the plasma, respectively. Vector \mathbf{G} is the gravity force but remains negligible in our study, and $n = \rho/m$ is the number density of protons, and m is proton mass, and we neglect the electron momentum. \mathbf{B} is the magnetic field vector; $\mathbf{E}_0 = 0$ is the exterior electric field on this system, which remains 0 in all our cases; η is a constant electric resistivity that is set to 0 in all cases, except one test case in section 3.1 for comparison purposes; \mathbf{J} is the electric current inversely calculated from its induction effect (Ampere's law): $\mathbf{J} = \frac{1}{\mu_0} \nabla \times \mathbf{B}$, where μ_0 is the vacuum permeability.

Equations (2-6) are solved numerically using the Michigan BATS-R-US code (Tóth et al., 2012), with a grid resolution of 0.05 R_E at the center.

3 Model Results

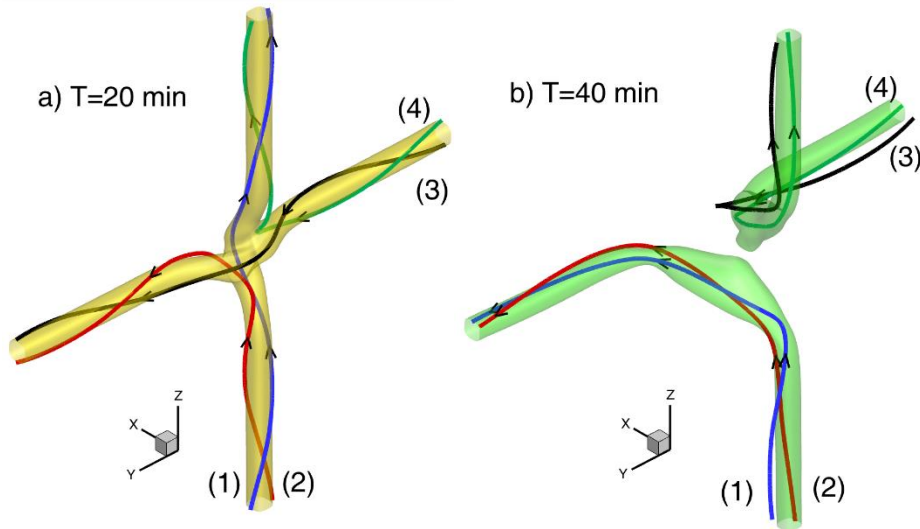
Magnetic reconnection involves large-scale evolution of magnetic topology and fine-scale diffusion. We carefully limit our discussion to the MHD regime, which describes the large-scale plasma dynamics and the magnetic topology, and leave the fine structure for future study.

A few tests have been launched to benchmark the evolution of our system: (1) By setting all $\mathbf{B} = 0$ for a hydrodynamic solution with no magnetic flux ropes, both boundary conditions result in stable laminar flow throughout the calculation domain. The shearing speed stays within less than 4 cells of the prescribed regions. This is expected because the Reynolds number is large in such a vacuum-like collisionless plasma. (2) We also run tests with only a single flux tube to evaluate the effect of the surrounding plasma on the tubes: tests applying the type A boundary condition result in a straight flux tube carried by the flow, while the type B boundary results in a flux tube bent and slipping at the boundaries. Although the plasma contained in each flux tube is given an initial velocity that matches the boundary conditions, they lose their momentum if the surrounding plasma is stationary.

The magnetic field strength during the Nov07 event is about 50 nT, resulting in an Alfvén speed of 350 km/s, and a proton gyro radius of 60km, or 0.01 R_E . However, because we initially

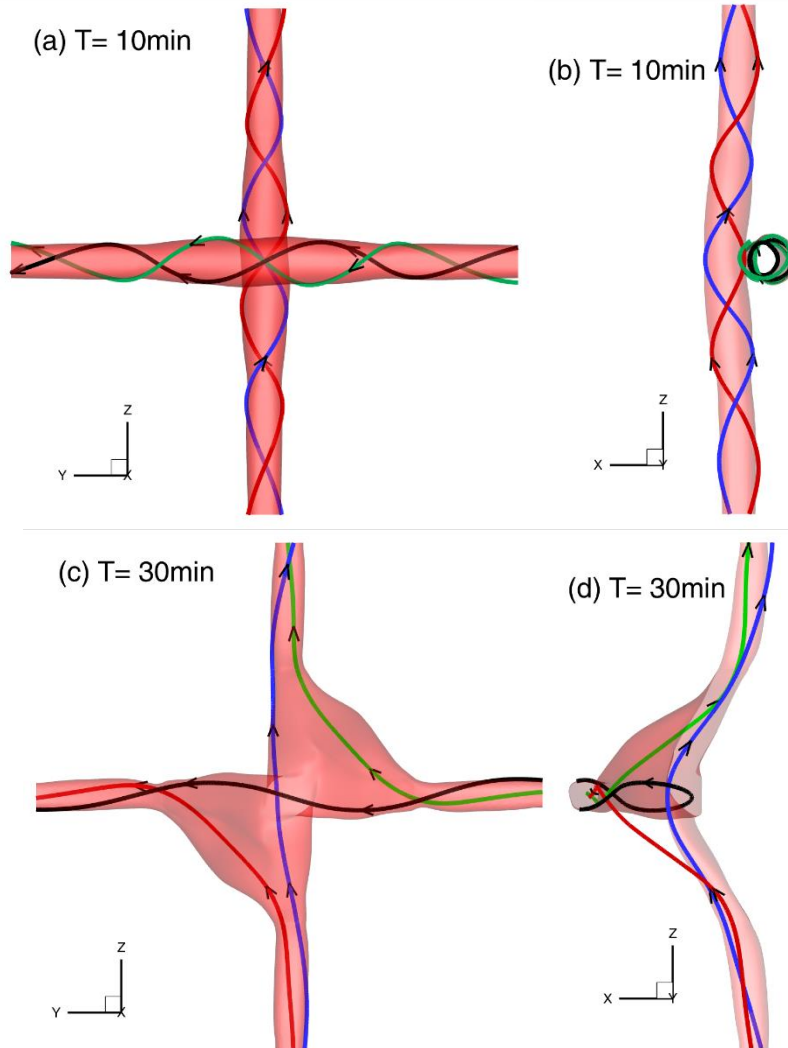
225 set $B=0$ outside the flux tubes, even with $0.05 R_E$ resolution, the flux ropes will dissipate during
 226 the simulation, so a flux rope with magnetic field strength as strong as this event cannot sustain
 227 in our simulation. Instead, even when we set the initial field strength to $B = 80$ nT, the magnetic
 228 field magnitude drops to about 4 nT with or without the entanglement interaction. Also, in cases
 229 A1 and A2, because the surface field is dissipating to the zero-field region, the magnetic $B\phi'$
 230 component decreases more quickly than the axial component, thus the flux ropes appear less
 231 “twisted” around the rope axis during the evolution. Our test shows that the field diffuses much
 232 more slowly in lower plasma temperatures (i.e., $T = 10^5$ K).
 233

234 3.1 Case A1, magnetic flux rope reconnection driven by dynamic pressure
 235



236 **Figure 2.** Case A1 results at two different times plotted in two different panels, respectively:
 237 Two 3-D field line plots of the simulated evolution of the entanglement. A colored surface of
 238 constant magnetic field magnitude (panel a, $B = 2$ nT; panel b, $B = 1.4$ nT) is plotted to estimate
 239 the location of the flux rope. In each of the plots, four representative field lines are traced in 3-D,
 240 color coded only so they are identifiable.
 241

242
 243 After the initial condition of case 1 shown in Figure 1a, the time evolution is revealed by
 244 Figure 2. As expected, most of the flux ropes are pushed by the flow at a constant speed, so the
 245 flux ropes remain straight except in the center region, where the entanglement happens. At $T=20$
 246 minutes, the footpoints of the flux tubes on the boundaries are at $\pm 1 R_E$, respectively. In the
 247 meantime, the bent segments of the two ropes extend $\pm 5 R_E$ in y and z coordinates, consistent
 248 with an Alfvén speed of 27 km/s. At 40 minutes, as shown in the right panel of Figure 2, the flux
 249 tubes did reconnect to form a new pair, comparable to what was sketched by Russell and Qi
 250 (2020).
 251



252

253
254

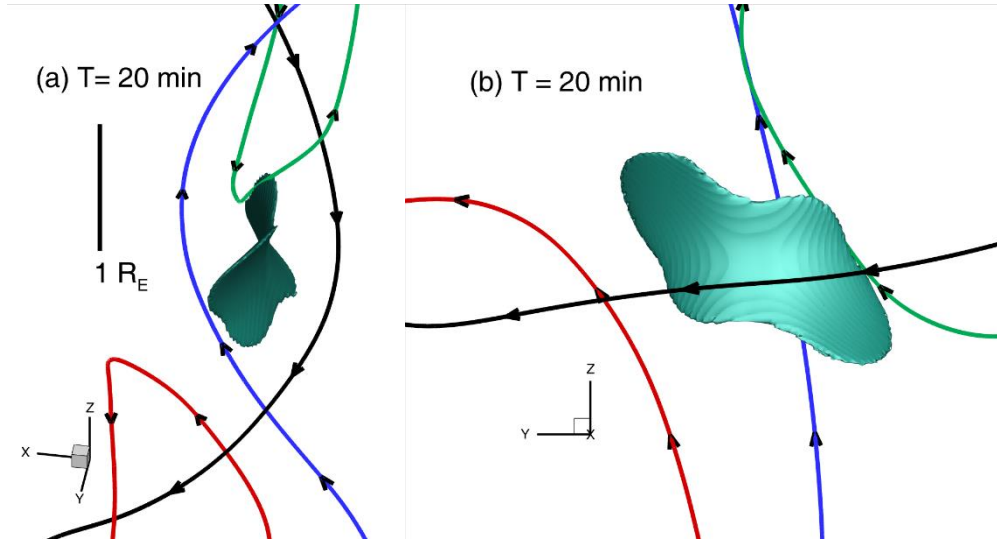
255 **Figure 3.** Case A1' results at early and late stages in 3-D plot from two different viewing angles.
256 Top panels are taken 10 minutes after initiation, while bottom panels are at 30 minutes. All
257 panels exhibit the entire $12.8 \times 12.8 R_E$ domain. In right panels (b) and (d), the iso-surfaces are cut
258 to show only the $y < 0$ half, while the field lines are traced in the full calculation domain. From
259 top to bottom, the values of the iso-surfaces are 5 nT and 3 nT, respectively.

260

261 Figure 3 shows the reconnection region in close-up snapshots during the evolution of the
262 flux rope-flux rope interaction. Case A1' is a special simulation launched with different settings
263 from the four cases listed in Table 1: We use a domain size of $12.8 \times 12.8 \times 12.8 R_E$, with a center
264 resolution of $0.025 R_E$, while the rest of the conditions remain the same as those of case A1. The
265 simulated evolution process remains similar to that of case A1, indicating that the grid resolution
266 is sufficient in our regular cases.

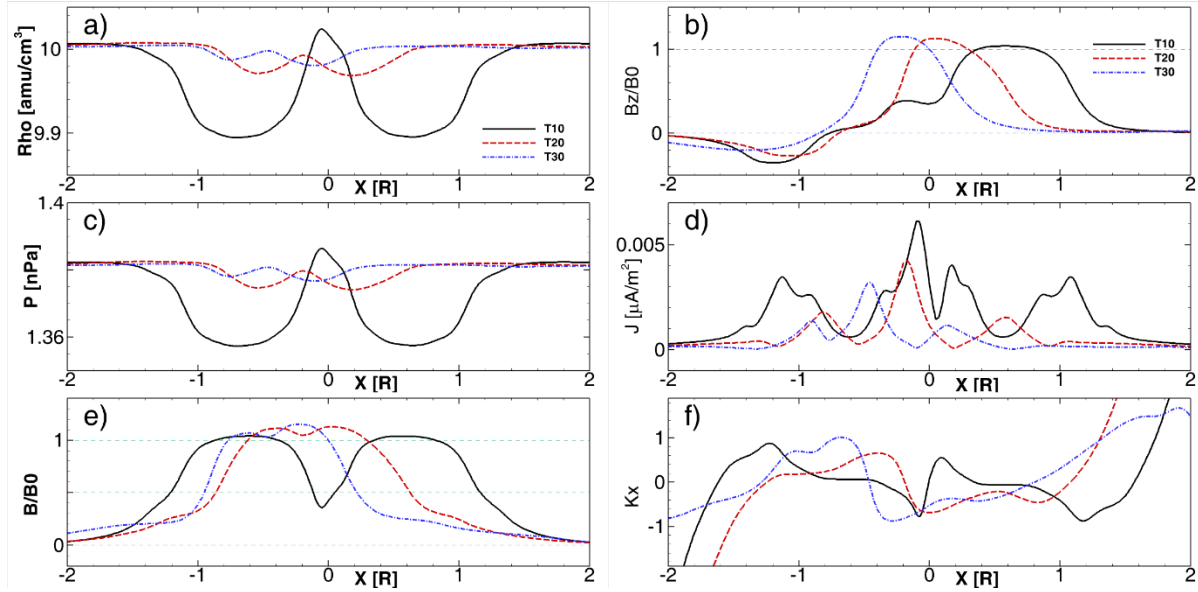
267 Panels a and b of Figure 3 show an early stage of this interaction. The ropes are slightly
268 bent by the entanglement interface, while most of the two ropes are not yet merged with each
269 other. Similar to the initial condition, the system is mostly symmetric in the x-y plane and the y-z
270 planes, respectively. There is a minor asymmetry at the center, arranged by the polarity of the

271 two tubes. In contrast, at $t = 30$ minutes, as shown in panels c and d of Figure 3, both ropes are
 272 highly bent within a radius of $4 R_E$, while newly connected lines recoil and expand the
 273 interaction region, making the system no longer symmetric. Compared with the stages at 10
 274 minutes in Figure 3 and 20 minutes in Figure 2, the tubes are now in the late stage of
 275 reconnection, with more than half of the flux being reconnected and moving in diagonal
 276 directions.
 277



278
 279 **Figure 4.** Case A1', a close up view of a same set of 3-D field lines in two different viewing
 280 angles at $T=20$ minutes. Iso-surface represents a current sheet with current density $J=0.004$
 281 $\mu\text{A}/\text{m}^2$. The vertical bar in panel a marks a scale of $1 R_E$, and both panels share the same length
 282 scale.
 283

284 To examine the diffusion region at the interface, the shape of the current sheet in the
 285 interaction region at $T=20$ minutes (middle stage) is plotted in Figure 4. The current is
 286 concentrated in a saddle-shaped layer, which is the expected shape of the interface when the two
 287 cylinders merge into each other. In the right panel, viewing along the x -axis, the asymmetry of
 288 the saddle caused by the direction of the magnetic field is revealed. In both close up views, two
 289 types of magnetic field curvature could show up in this region, depending on the trajectory of
 290 detectors: The reconnected lines bend away from the interface, while the piling up field lines
 291 bend toward the interface.
 292



293
 294 **Figure 5.** Case A1' result, variable values along the x-axis at three different times: 10 (solid
 295 lines), 20 (dashed lines), and 30 (dash-dotted lines) minutes after initiation. We note that scales
 296 for density and thermal pressure do not include the zero point, in order to exaggerate the
 297 variation. The magnetic B total and B_z component are normalized by a constant B_0 , which is the
 298 maximum value of B at $z = 2 R_E$ at that instant. In panel f, the 3-D curvature κ of the magnetic
 299 field is projected along the x-axis, which is approximately the normal of the central current sheet.
 300

301 Figure 5 shows the extracted values of density, plasma thermal pressure, normalized
 302 magnetic field intensity, magnetic B_z component, current intensity, as well as magnetic field
 303 curvature along the x-axis. Comparing panels a, c, and e, the thermal pressure variation
 304 associates well with the density, and anti-correlates with the variation of the magnetic field
 305 strength, indicating that the change in magnetic field is compensated by the plasma density.

306 Because the magnetic field is decreasing with time, to reveal the relative variation of the
 307 magnetic field, the field magnitude and B_z component are both normalized by the maximum
 308 value of B in the $z=2$ plane at the same time. We choose the $z=2$ plane to stay outside, but still as
 309 close as we can, to the compression region. In panel e of Figure 5, at $T=10$ minutes, the
 310 normalized B shows two humps, marking the location of the two ropes, barely merging into each
 311 other. At $T=20$ minutes, two ropes have merged significantly, and the normalized magnitude
 312 increased above 1 even in the central current sheet, indicating a compression of the magnetic
 313 field at this stage. At $T=30$ min, the two structures merged into one and shifted along the $-x$ -axis.

314 In panel b of Figure 5, the magnetic field B_z component crossed its zero value only once,
 315 and it is asymmetric about the $x = 0$ point, even though the x-axis crosses two flux ropes. The
 316 negative trench marks the azimuthal field of the evolved form of flux rope 2 from the initial
 317 condition, while the positive hump is the axial field of an evolved form of flux rope 1 in the
 318 initial condition.

319 In panel d of Figure 5, at $T = 10$ minutes, five peaks of current density are seen. The
 320 center peak is in the central current sheet, which is the reconnecting current sheet. The four
 321 smaller ones on both sides are the flux rope surface current associated with the core field. At
 322 $T=20$ minutes, two of the small peaks merge into the central current sheet, while the other two
 323 fold towards the center. At $T = 30$ minutes, the flux ropes are reconstructed, while the current

324 perturbations move anti-parallel to the x-axis. In general, the state variables do show the merging
 325 of two flux ropes, but the values depend highly on the trajectory.

326 The curvature of magnetic field lines are defined as $\boldsymbol{\kappa} = \mathbf{b} \cdot \nabla \mathbf{b}$, where $\mathbf{b} = \mathbf{B}/B$ is a unit
 327 vector along the magnetic field. As shown in Figure 4, the current sheet normal is mainly along
 328 the x-axis, so we choose $\boldsymbol{\kappa}_x$ to show the magnetic field curvature in panel f of Figure 5. At T=10
 329 minutes, the curvature shows two pairs of bipolar signatures, consistent with the transverse
 330 crossing of the two unmerged flux ropes. Later at T=20 and 30 minutes, as is plotted in 3-D in
 331 Figures 3 and 4, and observed by Qi et al. (2020), the field lines, instead of curving towards the
 332 individual flux rope axes, do curve towards the central current sheet, consistent with the picture
 333 that the two ropes are actively pulling against each other.

334 To further investigate the conditions for reconnection, the following tests have been
 335 performed but are not plotted here: By removing the Hall terms from the Hall-MHD equations
 336 (2-6), and setting $\eta = 0.005$ (Birn et al., 2001), the reconnection process is similar to that shown
 337 in Figure 2, consistent with this high beta condition that flow drives the magnetic field
 338 reconnection. Even with no Hall terms or constant resistivity, the reconnection still occurred via
 339 numerical diffusion. To confirm the effect of beta, we launched test case A1b, with the only
 340 difference from the case A1 condition being the plasma temperature of 10^5K , which is the
 341 interplanetary solar wind condition instead of the nominal magnetosheath value. Not shown here,
 342 the two tubes remain entangled after 50 minutes from release, indicating that even with Hall
 343 MHD, the reconnection rate is insufficient to reconnect the amount of flux in such low beta
 344 conditions.

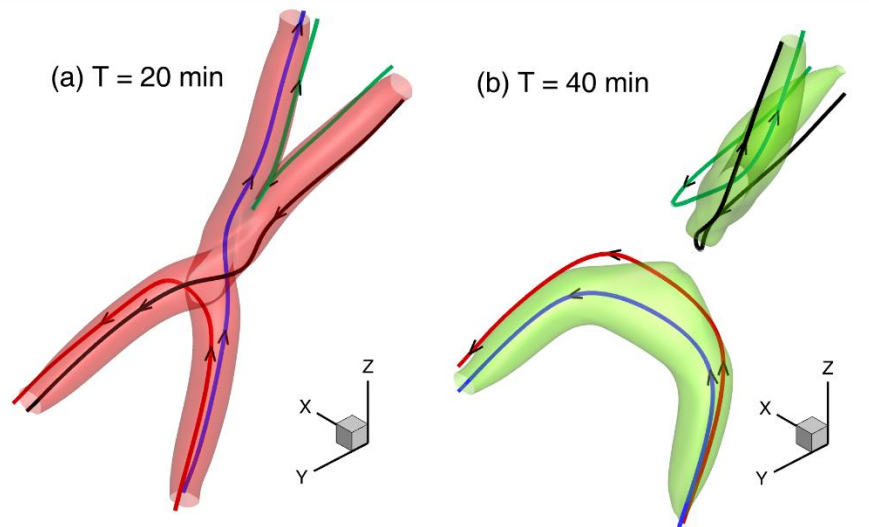
345

346 3.2 Case A2, magnetic flux tube reconnection driven by dynamic pressure

347

348 With the case A boundary conditions and the case 2 initial conditions, case A2 is
 349 modeled in the same grid system as that of case A1. As shown in Figure 6, the reconnection of
 350 flux tubes is complete after 40 minutes, comparable with that of case A1. In addition, compared
 351 with case A1, both initial conditions result in a small magnetic $B\phi'$ component, so the observed
 352 helicity in the flux ropes may come from other processes.

353



354

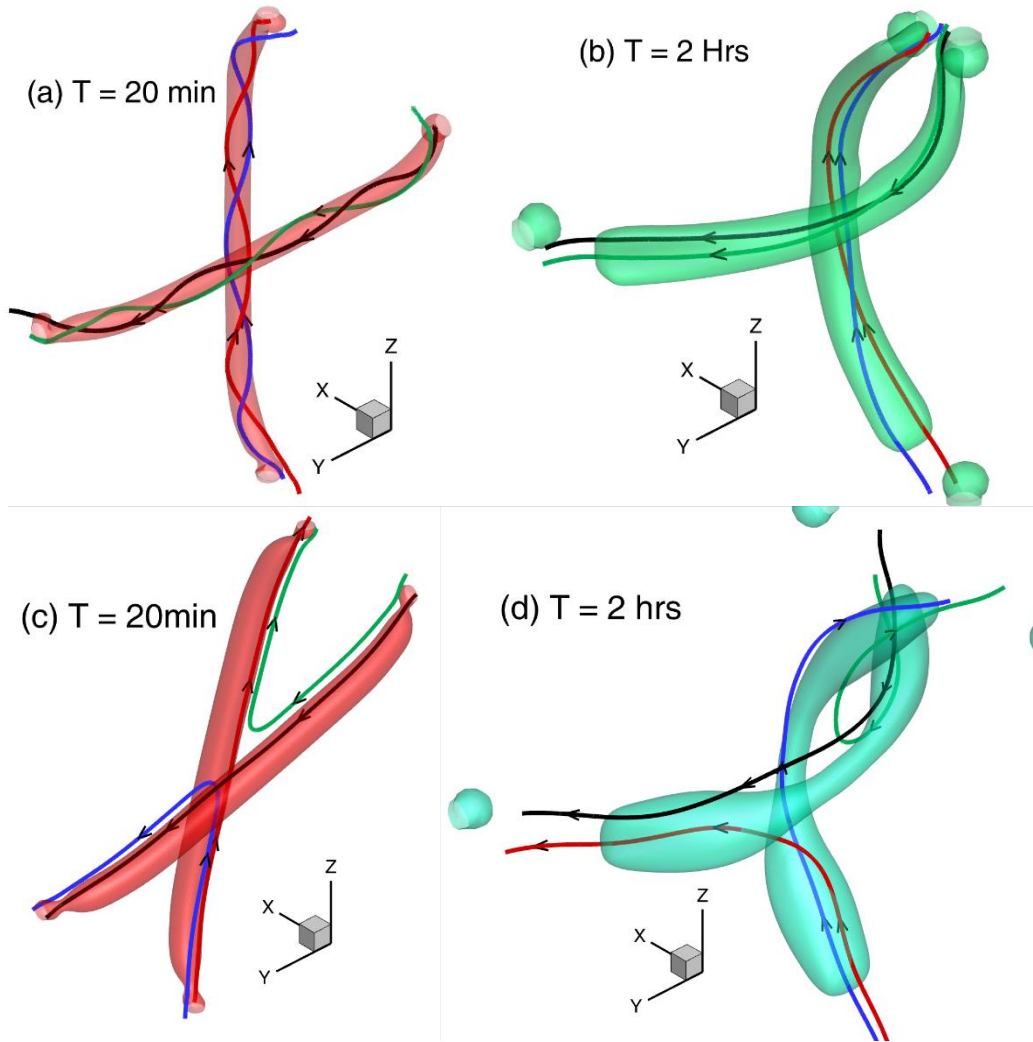
355 **Figure 6.** Case A2, interaction of two flux tubes driven by the flow. Shown are 3-D plots at the
356 same viewing angle as that of Figure 2, with a surface marking the region with a non-negligible
357 magnetic field. Four representative magnetic field lines are traced in 3-D to show the topology of
358 the magnetic field during the interaction. Left panel: Iso-surface at $B=4$ nT at 20 minutes after
359 initiation. Right panel: Iso-surface of $B=1.6$ nT at 40 minutes after release.
360

361 For this type 2 initial condition, both flux tubes are tilted by an artificial angle of 16.7° .
362 We have launched two test runs to investigate the effect of this angle: Case B10, with this tilting
363 being 0 rad, the reconnection still occurs with a similar process. Case B13, with the tilt being
364 -16.7° , the reconnection evolves more slowly, because it took the two tubes, defined by the
365 magnitude of the magnetic field, over 50 minutes to become mostly reconnected and separated.
366 Earlier, using the same BATS-R-US code but not including the Hall terms nor uniform resistivity,
367 Jia et al. (2007) have found no significant reconnection when two regions with magnetic field
368 perpendicular to each other are merging in a nominal solar wind condition. Together with Case
369 A1b, we speculate that the difference in the effectiveness of reconnection at different guide field
370 percentages relies on the plasma temperature, or effectively, the plasma β , awaiting more
371 detailed investigation to confirm.
372

373 3.3 Cases B1 and B2, interactions driven only by magnetic tension force

374
375 The time evolution of initial conditions type 1 and 2 are simulated again by pairing with
376 the type B boundary condition. The results are shown in Figure 7. Even after two hours, neither
377 ropes or tubes are fully reconstructed. For both cases, the drag from the side boundaries are
378 insufficient to reconnect the flux ropes/tubes, even though weak reconnection occurred in weak
379 field regions surrounding the flux ropes/tubes. The spherical structures shown in iso-surfaces
380 close to the boundaries are footpoints of the flux tubes, driven by the boundary conditions. They
381 appear disconnected from the central segment of the iso-surface at $T=2$ hours, indicating the
382 diffusion mainly happened here close to the boundaries. Even in this highly diffusive plasma, the
383 reconnection rate driven by the tension force passed along the flux tubes from the boundaries, is
384 not fast enough for the two tubes to reform before the two ends pulled by the boundaries travel
385 too far. Thus most of the energy is lost close to the boundaries, instead of reconnecting in the
386 center.

387 As we did in sections 3.1 and 3.2, we run cases B1 and B2 again with plasma temperature
388 $T=10^5$ K. As expected, the reconnection rate is not fast enough for the two tubes to reform,
389 although the diffusion of the tubes seems slower. Thus the flux tubes/ropes remain entangled but
390 the magnetic field strength piles up to too high at the interface to significantly decrease our
391 simulation time step, and the simulation would not proceed. Since a plasma temperature of
392 $T=10^5$ K may not apply to the plasma conditions in the magnetosheath, further investigation with
393 this parameter is out of the scope of this study.



394

395

396

397

398

399

400

Figure 7. 3-D plot of cases B1 and B2 results in the same viewing angle as used in Figures 2 and 6. Top panels show the results of case B1, while the results of case B2 are shown at the bottom. Left panels show 20 minutes with iso-surface of magnetic field magnitude $B=3$ nT, while right panels show time = 2 hours, with iso-surface $B=1$ nT.

401

4 Discussion and Conclusions

402

403

404

405

406

407

408

409

4.1 Evaluation of parameters chosen

410

411

412

Comparing cases A1 and A2, we have found that the reconnection is fast enough for the two tubes, whether originally with or without twist, to reconnect in 40 minutes. In reality, this is

413 close to the amount of time for a magnetic flux tube to travel from the day side to the night side,
414 so an upper limit of 40 minutes is a good estimate of whether the reconnection of flux tubes will
415 occur in our model or not.

416 We admit that the selection of the velocity of 13km/s is arbitrary. In contrast, the flow
417 vortex around FTEs is usually on the same order (Zhang et al., 2011), while the flow speed that
418 carries this entangled structure is one order of magnitude greater during the Nov07 event. The
419 flow fluctuations during this event are also about 100km/s, giving an upper limit to the relative
420 velocity between two flux tubes. Our test shows that this relative speed will affect the speed of
421 evolution; a relative speed of 26 km/s results in a completion of reconnection in 20 minutes.
422 Hence, for a speed at this magnitude, the plasma condition is sufficient for a reconnection to
423 occur, and fast enough to reconnect the magnetic flux in tens of minutes.

424 During reconnection, the peak magnetic field strength drops to about 3 nT. Although in
425 reality a 50 nT field is measured, the total flux enclosed in a 50 nT flux rope of $0.1 R_E$ radius is
426 comparable to the total flux in our 3nT flux rope with a $0.4 R_E$ radius, indicating that our result is
427 applicable to real flux tube/rope reconnections interpreted from MMS observations. On the other
428 hand, such field diffusion may be constrained by tweaking the thermal pressure balance across
429 the tubes, and we leave this study to future modelers.

430 On the other hand, by comparing the results from type A and type B boundary conditions,
431 despite the diffusion of this high- β plasma in our simplified simulation, we find that this
432 reconnection, if it happens, would be driven by the dynamic pressure of the ambient flow,
433 instead of tension from distant locations.

434 For cases with type A boundaries, the disturbance stays within $\pm 5 R_E$, which is the region
435 in which we are assuming uniformity. Nonetheless, a more complicated real situation may exist
436 at this scale, i.e., the flux tubes could be bent, both the field strength and helicity of the flux tubes
437 may vary along their axis, and the entangled flux tubes may undergo other processes when they
438 move through the plasma in the magnetosheath before they collide with each other.

439 In equation (1), we adopted a parameter H to represent the sign of helicity of the flux
440 ropes in our initial conditions, and it was set to 1 in all flux rope cases. We run case A1 again
441 with $H = -1$ in flux rope #2, and the evolution process is comparable to the case A1 result. The
442 relative polarity of the axial field also does not matter to the timing of reformation: We have
443 reversed the axial field of flux rope #2, the flux ropes rematches to form new pairs, and the
444 asymmetric extended interaction region has changed accordingly, but the general process evolves
445 with similar timing. Further, in all cases, we have assumed symmetric entanglement, where the
446 magnetic fields in the two flux tubes share the same magnitude. From our model result, we
447 would expect the stronger one to cut through the weaker one, but more simulations are needed to
448 confirm our speculation. We have also assumed symmetry between the two ends of a flux tube.
449 In reality, they may not only be bent, but also sitting in plasmas of different states, and moving at
450 different speeds. In contrast to the guide field study with case A2, for case A1 we have assumed
451 perpendicular interaction between two ropes. Combined with chirality and polarity of the flux
452 ropes, how does this angle affect the result? These above possibilities call for more local models,
453 to probe with more conditions and wider range of parameters, as well as global models with
454 resolution sufficiently fine and self-consistently generating such interactions.

455

456 4.2 Application to multiple scenarios

457

458 In section 2, we noted that we simulate the evolution from stages b to c by Russell and Qi
459 (2020), i.e., when two flux tubes became entangled, and reconnection at the interface eventually
460 disentangled them to form a new pair. We emphasize that the generation of entangled flux tubes,
461 i.e., how the solar wind-magnetosphere interaction evolved from stages a to b by Russell and Qi
462 (2020), is not the scope of this study. requires global models and is not the scope of this study:
463 We have chosen our approach based on the observation of entangled flux tubes. After
464 reconnection, the tubes should move freely with the plasma until they reach another obstacle, but
465 the geometry would be different from what we are simulating here, and is left for future study.

466 Flux rope interactions have been studied for decades in the solar corona, as recently
467 reviewed for models by Keppens et al. (2019), and for observations by Liu (2020). Such
468 interactions are ubiquitous on the solar surface, and correlated to multiple observations of
469 phenomena, including filaments, prominences, and the release of coronal mass ejections (CMEs).
470 For flux rope interactions in a typical low-beta solar corona, a related study has been performed
471 using a 3-D resistive MHD model. When investigating the interaction of two flux ropes of
472 various relative angle, helicity, and polarity, Linton et al. (2001) used a solenoidal velocity field
473 to find many different interaction modes, among which, their “slingshot mode” that reconnects
474 into two new ropes is the most comparable with our case A1 result, also supporting the
475 feasibility of flux rope reconnection in general. Our Hall MHD model on the other hand, after
476 changes in parameters and conditions, may apply to the coronal environment for flux rope
477 interactions, and more sophisticated arch twisting evolutions (i.e., Török et al., 2005).

478 Last, the real solar wind-magnetosphere interaction might be patchy and sporadic at this
479 sub- R_E scale. As stated in the introduction, despite the large amount of literature that envisions
480 such entanglement of flux tubes from both theory and observations, we do also observe a
481 noticeable amount of literature that explains FTEs otherwise, including the events observed by
482 the MMS (Qi et al., 2020).

483 In summary, our study presents a reconnection process of two flux ropes/tubes in the Hall
484 MHD regime, driven by ambient plasma flow of the magnetic sheath conditions. Our model
485 visualizes the evolution of the interaction region, and predicts the encountering of opposite
486 magnetic curvature along different trajectories. Based on model results, we recommend surveys
487 in the MMS magnetic field data to reconstruct the 3-D shape of early and late stages of the flux
488 rope/tube entanglement, using the plasma data as an indication of connectivity to confirm the
489 stages. Finally, we emphasize that application of our idealized model should apply not only to
490 magnetospheric reconnection, but also to flux rope interactions in the solar corona.

491

492 **Acknowledgments, Samples, and Data**

493

494 The BATS-R-US code used in the study is available via the NASA Community Coordinated
495 Modeling Center (CCMC) website: <https://ccmc.gsfc.nasa.gov/models/index.php>.

496 **References**

- 497 Birn, J., Drake, J.F., Shay, M.A., Rogers, B.N., Denton, R.E., Hesse, M., Kuznetsova, M., Ma,
 498 Z.W., Bhattacharjee, A., Otto, A., & Pritchett, P.L. (2001), Geospace environmental modeling
 499 (GEM) magnetic reconnection challenge. *J. Geophys. Res.*, 106 (A3), 3715–3720.
- 500 Burch, J. L., Moore, T. E., Torbert, R. B., & Giles, B. L. (2015), Magnetospheric Multiscale
 501 Overview and Science Objectives. *Space Science Reviews*, 199(1–4), 5–21.
 502 <https://doi.org/10.1007/s11214-015-0164-9>
- 503 Dorelli, J. C., & Bhattacharjee, A. (2009), On the generation and topology of flux transfer
 504 events. *Journal of Geophysical Research: Space Physics (1978–2012)*, 114(A6).
 505 <https://doi.org/10.1029/2008ja013410>
- 506 Fear, R. C., Milan, S. E., Fazakerley, A. N., Lucek, E. A., Cowley, S. W. H., & Dandouras, I.
 507 (2008), The azimuthal extent of three flux transfer events. *Ann. Geophys.*, 26(8), 2353-2369.
 508 doi:10.5194/angeo-26-2353-2008
- 509 Fedder, J. A., Slinker, S. P., Lyon, J. G., & Russell, C. T. (2002), Flux transfer events in global
 510 numerical simulations of the magnetosphere. *J. Geophys. Res.: Space Physics*, 107(A5).
 511 doi:10.1029/2001JA000025
- 512 Hesse, M., Birn, J., & Schindler, K. (1990), On the topology of flux transfer events. *Journal of*
 513 *Geophysical Research*, 95(A5), 6549. <https://doi.org/10.1029/ja095ia05p06549>
- 514 Imber, S. M., Slavin, J. A., Boardsen, S. A., Anderson, B. J., Korth, H., McNutt, R. L., &
 515 Solomon, S. C. (2014), MESSENGER observations of large dayside flux transfer events: Do
 516 they drive Mercury's substorm cycle? *J. Geophys. Res.: Space Physics*, 119(7), 5613-5623.
 517 doi:10.1002/2014JA019884
- 518 Jia, Y.-D., Combi, M. R., Hansen, K. C., & Gombosi, T. I. (2007), A global model of cometary
 519 tail disconnection events triggered by solar wind magnetic variations. *J. Geophys. Res.*,
 520 112(A5). doi:10.1029/2006JA012175
- 521 Keppens, R. Guo, Y., Makwana, K., Mei, Z., Ripperda, B., Xia, C., Zhao, X. (2019), Ideal MHD
 522 instabilities for coronal mass ejections: interacting current channels and particle acceleration.
 523 *Reviews of Modern Plasma Physics*, 3(1), id.14. doi:10.1007/s41614-019-0035-z
- 524 Lee, L. C., & Fu, Z. F. (1985), A theory of magnetic flux transfer at the Earth's magnetopause.
 525 *Geophysical Research Letters*, 12(2), 105–108. <https://doi.org/10.1029/gl012i002p00105>
- 526 Linton, M. G., Dahlburg, R. B., & Antiochos, S. K. (2001), Reconnection of Twisted Flux Tubes
 527 as a Function of Contact Angle. *Astrophys. J.*, 553(2), 905-921. doi:10.1086/320974
- 528 Liu, R. (2020), Magnetic Flux Ropes in the Solar Corona: Structure and Evolution toward
 529 Eruption, *Research in Astron. Astrophys.*, in press, arXiv:2007.11363
- 530 Liu, Z. X. & Hu, Y. D. (1988), Local magnetic reconnection caused by vortices in the flow field.
 531 *Geophys. Res. Lett.*, 15, 752–755. doi:10.1029/GL015i008p00752.
- 532 Lundquist, S. (1950), Magneto-hydrostatic fields. *Ark. Fys.*, 2, 361–365.
- 533 Øieroset, M., Phan, T. D., Drake, J. F., Eastwood, J. P., Fuselier, S. A., & Strangeway, R. J., et
 534 al. (2019), Reconnection with Magnetic Flux Pileup at the Interface of Converging Jets at the
 535 Magnetopause. *Geophysical Research Letters*, 46(4), 1937–1946.
 536 <https://doi.org/10.1029/2018gl080994>
- 537 Otto, A. (1991), Three-dimensional magnetohydrodynamic simulations of processes at the
 538 earth's magnetopause. *Geophysical & Astrophysical Fluid Dynamics*, 62(1–4), 69–82.
 539 <https://doi.org/10.1080/03091929108229126>

- 540 Pu, Z. Y., Raeder, J., Zhong, J., Bogdanova, Y. V., Dunlop, M., & Xiao, C. J., et al. (2013),
541 Magnetic topologies of an in vivo FTE observed by Double Star/TC-1 at Earth's
542 magnetopause. *Geophysical Research Letters*, 40(14), 3502–3506.
543 <https://doi.org/10.1002/grl.50714>
- 544 Qi, Y., Russell, C. T., Jia, Y.-D., Hubert, M. (2020), Temporal Evolution of Flux Tube
545 Entanglement at the Magnetopause as Observed by the MMS Satellites, submitted to
546 *Geophysical Research Letters*, available at: <https://doi.org/10.1002/essoar.10504155.1>
- 547 Raeder, J. (2006), Flux transfer events: 1. Generation mechanism for strong southward IMF.
548 *Ann. Geophys.*, 24(1), 381–392.
- 549 Russell, C. T. & Elphic, R. C. (1979), ISEE observations of flux transfer events at the dayside
550 magnetopause. *Geophysical Research Letters*, 6(1), 33–36.
551 <https://doi.org/10.1029/gl006i001p00033>
- 552 Russell, C. T. & Qi, Y. (2020), Flux Ropes Are Born in Pairs: An Outcome of Interlinked,
553 Reconnecting Flux Tubes. *Geophysical Research Letters*.
554 <https://doi.org/10.1029/2020gl087620>
- 555 Southwood, D. J., Farrugia, C. J., & Saunders, M. A. (1988), What are flux transfer events?
556 *Planetary and Space Science*, 36(5), 503–508. [https://doi.org/10.1016/0032-0633\(88\)90109-2](https://doi.org/10.1016/0032-0633(88)90109-2)
- 557 Tan, B., Lin, Y., Perez, J. D., & Wang, X. Y. (2011), Global-scale hybrid simulation of dayside
558 magnetic reconnection under southward IMF: Structure and evolution of reconnection.
559 *Journal of Geophysical Research: Space Physics (1978–2012)*, 116(A2),
560 <https://doi.org/10.1029/2010ja015580>
- 561 Tóth, G., Ma, Y.J., & Gombosi, T. I. (2008), Hall magnetohydrodynamics on block-adaptive
562 grids. *J. Comp. Phys.*, 227(14), 6967–6984. doi:10.1016/j.jcp.2008.04.010
- 563 Tóth, G., van der Holst, B., Sokolov, I. V., De Zeeuw, D. L., Gombosi, T. I., Fang, F.,
564 Manchester, W. B., Meng, X., Najib, D., Powell, K. G., Stout, Q. F., Glocer, A., Ma, Y.J., &
565 Opher, M. (2012), Adaptive numerical algorithms in space weather modeling, *J. Comp. Phys.*,
566 231(3), 870–903. doi:10.1016/j.jcp.2011.02.006
- 567 Zhang, H., Kivelson, M., Angelopoulos, V., Khurana, K., Walker, R., Jia, Y.-D., McFadden, J.,
568 & Auster, U. (2011), Flow Vortices Associated with FTEs Moving along the Magnetopause:
569 Observations and an MHD Simulation, *J. Geophys. Res.*, 116, A08202.
570 doi:10.1029/2011JA016500.
- 571 Zhao, C. (2019), Statistical Study on Two Types Of Flux Transfer Events Observed By MMS
572 Spacecraft. UCLA. ProQuest ID: Zhao_ucla_0031D_17883. Merritt ID:
573 ark:/13030/m5zd31z9. Retrieved from <https://escholarship.org/uc/item/5jb369td>
574